Vol. 23, No. 3(2024) Mat24292
Revista Mexicana de Ingeniería Química

# An improved method for $CO_2$ adsorption based on two precursors supported in a mesoporous silica

# Método mejorado para adsorción de $CO_2$ basado en dos precursores con soporte de silica mesoporosa

M.I. González-Nava[1]* R. Nava-Mendoza[1]*, R. Velazquez-Castillo[1], J.D. Mendiola-Santibañez[1], E.M. Rivera-Muñoz[2], J. Rodriguez-Resendiz[1]

[1] *Division of Research and Postgraduate Faculty of Engineering, Autonomous University of Queretaro, Queretaro.76010, Mexico.*

[2] *Center for Applied Physics and Advanced Technology, National Autonomous University of Mexico, AP 1-1010, Querétaro, 76010, Mexico.*

Received: Match 11, 2024; Accepted: July 8, 2024

## Abstract

The escalating levels of $CO_2$ in recent years have demanded effective solutions and technologies for emissions reduction. The $CO_2$ capture, storage, and transformation allow the opportunity to reduce emissions into the atmosphere and thus mitigate related problems. This study explores novel methods for enhancing the adsorption and removal of $CO_2$ using mesoporous materials. Our approach involves impregnating mesoporous silica SBA-15 with varying proportions (5%, 10%, and 15%) of calcium and magnesium acetate precursors, as well as their oxides and hydroxides. Preliminary experiments showed that magnesium demonstrated superior performance, leading to further investigation using a secondary precursor, magnesium chloride. Subsequent analysis of $CO_2$ adsorption revealed enhanced results with magnesium oxides and hydroxides derived from this second precursor. The findings indicate that optimal adsorption is achieved with 15% $Mg(OH)_2$, 8.09 $\frac{mmol}{g}$, and 15% MgO, 10.12 $\frac{mmol}{g}$, when employing the magnesium chloride precursor. Notably, adsorption increases proportionally with higher material ratios. These results surpass existing literature, showcasing the efficacy of the proposed methodology in achieving superior $CO_2$ adsorption.

*Keywords*: Adsorption of $CO_2$, oxides, hydroxides, mesoporous silica, acetates, chloride.

## Resumen

Los niveles crecientes de $CO_2$ en años recientes requieren soluciones efectivas y tecnologías para reducción de emisiones. La captura, almacenamiento y transformación de $CO_2$ abren oportunidad de reducir emisiones a la atmósfera y por lo tanto de mitigar los problemas relacionados. Este estudio explora métodos de vanguardia para mejorar la adsorción y remoción de $CO_2$ por medio de material mesoporoso. Nuestro enfoque supone impregnar material de silica mesoporosa SBA-15 con distintas proporciones (5%, 10%, and 15%) de precursores de acetato de magnesio y calcio, así como de sus óxidos e hidróxidos. Experimentos preliminares demuestran el desempeño superior del magnesio, conduciendo a más investigaciones usando un precursor secundario, cloruro de magnesio. Un análisis posterior de la adsorción de $CO_2$ ha revelado resultados mejorados con óxidos e hidróxidos de magnesio derivados del segundo precursor. Los resultados indican una adsorción optima con 15% $Mg(OH)_2$, 8.09 $\frac{mmol}{g}$, y 15% MgO, 10.12 $\frac{mmol}{g}$ si se usa cloruro de magnesio como precursor. La adsorción es notable y aumenta proporcionalmente a la cantidad de material. Los resultados superiores sobrepasan la literatura existente y demuestran la eficacia de la metodología propuesta.

*Palabras clave*: Adsorción de $CO_2$, óxidos, hidróxidos, silica mesoporosa, acetatos, cloruro.

* *Corresponding author. E-mail*: mgonzalez304@alumnos.uaq.mx; rufino@uaq.mx;
https://doi.org/10.24275/rmiq/Mat24292
*ISSN*:1665-2738, *issn-e*: 2395-8472

# 1 Introduction

Failure to drastically decrease carbon emissions poses a significant threat to our planet, given the continuous rise in atmospheric carbon dioxide ($CO_2$) levels over the years. As of 2021, global $CO_2$ concentrations have reached yet another high record (Guo *et al*., 2022). The ongoing economic development and increased human activities result in extensive fossil fuel consumption and a persistent surge in coal concentration. Consequently, developing $CO_2$ conversion technologies becomes imperative to mitigate greenhouse gas emissions (Chen *et al*., 2022; Dong *et al*., 2023; Maruccia *et al*., 2021, Guo *et al*., 2022; Mohamedali *et al*., 2020, Akram *et al*., 2022; de Sá da Silva *et al*., 2022; Wu *et al*., 2022; Ai *et al*., 2023; Vakros *et al*., 2023; Arbi *et al*., 2023).

Currently there are different methods to absorb pollutants that affect water, air and the entire environment (Villabona-Ortíz *et al*., 2019, 2021; Tovar *et al*., 2020, 2021; Dávila-Parra, *et al*., 2022; Gonzales-Condori, 2023).

A practical approach involves capturing carbon at its source and securely storing it. $CO_2$ capture separates carbon dioxide from other gases generated during combustion in thermal power plants, oil refineries, cement manufacturing, and the steel industry (Al-Absi *et al*., 2022). Once separated, the captured $CO_2$ is transported and injected into deep geological formations, other uses of captured $CO_2$ besides geological storage, thereby reducing atmospheric emissions (de Sá da Silva *et al*., 2022).

The transformation of $CO_2$ involves chemical conversion using alkaline adsorbents, forming stable, water-insoluble calcium and magnesium carbonates, an environmentally sustainable approach to permanent $CO_2$ storage (Liu and Gadikota, 2018).

Various alkaline adsorbents, including simple metal oxides (e.g., CaO, MgO), and hydroxides (e.g., $Ca(OH)_2$, $Mg(OH)_2$ and NaOH), have been proposed for gas-solid carbonation (Al-Absi *et al*., 2022). These nanoparticles consist on particles of common metals with sizes smaller than microns, falling within the nanometric scale (Dong *et al*., 2023).
Calcium hydroxide can be used as a reagent (Vance, 2015). Mineral carbonation involves the reaction of $CO_2$ with metal oxides, such as magnesium and calcium oxide, to form carbonates (Dong *et al*., 2023;Al-Absi *et al*., 2022; Wu *et al*., 2022).

Calcium and magnesium hydroxides and oxides are silicate minerals that are relatively abundant worldwide and serve as an attractive feedstock for $CO_2$ mineralization. In this context, the material known as SBA-15 (Santa Barbara Amorphous No. 15), initially developed by Stucky, exhibits a high surface area. The material known as SBA-15 (Santa Barbara Amorphous No. 15), initially developed by Stucky, exhibits a high surface area and a hexagonal structure with uniform pores resembling a honeycomb. Additionally, it can be tailored with a wide range of pore sizes (4.6 nm to 30 nm) surface area (800-940 $\frac{m^2}{g}$), pore volume ($\frac{m^3}{g}$) and pore wall thicknesses (3.1 nm to 6.4 nm), achieved by adjusting synthesis parameters such as temperature (35 ºC to 140 ºC) and reaction time (11 h to 72 h). SBA-15's favorable textural properties make it suitable for incorporating hydroxide and metal oxide nanoparticles on its surface (Qin, 2023) ensuring high dispersion and generating more active adsorbents for the carbonation reaction (Mohanned, 2020).
This study aims to develop $CO_2$ adsorbent materials based on short-sized mesoporous silicas of the SBA-15 type impregnated with nanoparticles of calcium and magnesium hydroxides and metal oxides. Two different precursors, acetate and chloride, capture and convert $CO_2$.
Authors propose the development of $CO_2$ adsorbent materials based on SBA-15 mesoporous silicas decorated with nanoparticles of calcium and magnesium hydroxides and metal oxides to capture and convert $CO_2$ through mineral carbonation.The impregnation of mesoporous silica SBA-15 with calcium and magnesium acetates, oxides, and hydroxides in proportions of 5%, 10%, and 15% reveals superior results for magnesium. Subsequently, magnesium chloride served as a second precursor, enhancing $CO_2$ adsorption by acquiring magnesium oxides and hydroxides in advance, yielding improved results. Notably, optimal adsorption occurs with 15% $Mg(OH)_2$ (8.09 $\frac{mmol}{g}$) and 15% MgO (10.12 $\frac{mmol}{g}$) when using the magnesium chloride precursor.
The results surpass existing literature, showcasing the efficacy of the proposed methodology in achieving superior $CO_2$ adsorption. This work demonstrates that incorporating $Mg(OH)_2$, CaO, $Ca(OH)_2$, and MgO nanoparticles on the surface of the SBA-15 mesopore matrix generates adsorbents with a notable capacity for $CO_2$ adsorption and conversion to $CaCO_3$ through the carbonation reaction.
The resulting materials, $CaCO_3$-SBA-15 and $MgCO_3$-SBA-15, can be integrated into cementitious formulations for various applications. The outcomes presented herein surpass those reported in the literature, affirming the potential of $CO_2$ adsorption to contribute positively to environmental preservation. Furthermore, designing filters utilizing these adsorbent materials directly from companies' gaseous emissions (adsorption of $CO_2$ and its conversion to $CaCO_3$) presents a compelling alternative for reducing $CO_2$ emissions, enhancing our air quality.

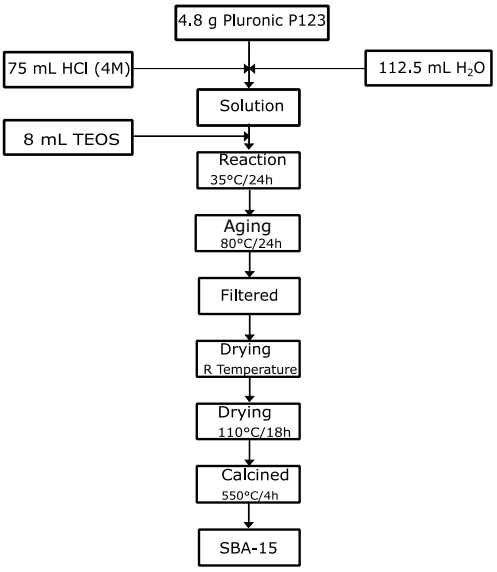


Figure 1. Synthesis of ordered mesoporous silica material SBA-15.

## 2 Materials and Methods

### 2.1 *Synthesis of ordered mesoporous silica material SBA-15.*

The mesoporous silica material SBA-15 was synthesized using the Sol-Gel process, employing a neutral surfactant, Pluronic P123, as the guiding agent for the meso-structure. To initiate the process, P123 was dissolved in a solution of hydrochloric acid and deionized water with constant stirring at 35°C, posteriorly the Sol-Gel process was initiated by adding the silica precursor, tetraethoxysilane (TEOS). The reaction was allowed to proceed for 24 hours with continuous agitation. Following the reaction, the maturation process was conducted by transferring the gel obtained into a polypropylene container, covering it, and placing it in a muffle for 24 hours at 80°C without agitation. After completion, the material was allowed to cool, and the solid product was recovered through filtration. Subsequently, it dried at room temperature, followed by further drying at 110°C for 18 hours at a heating rate of 2 $\frac{^{\circ}C}{min}$. Finally, calcination was conducted at 550°C for 4 hours with a heating rate of 1 $\frac{^{\circ}C}{min}$. This process effectively eliminated the organic base, yielding the mesoporous silica structure as the sole product (Vance *et al*., 2015) the process is described in figure 1.

### 2.2 *Incorporation of $Ca(OH)_2$ and $Mg(OH)_2$ nanoparticles into SBA-15.*

To incorporate calcium hydroxide ($Ca(OH)_2$) and magnesium hydroxide ($Mg(OH)_2$) nanoparticles onto the surface of short-sized mesoporous silica SBA-15, the pore filling impregnation method (incipient wetting) was employed. Aqueous solutions of calcium (II) acetate dihydrate $Ca(OH)_2 \bullet 2H_2O$ (Sigma-Aldrich) and magnesium (II) acetate dihydrate $Mg(OH)_2 \bullet 2H_2O$ (Sigma-Aldrich) served as sources for calcium and magnesium (II) hydroxides. The deposition amounts of $Ca(OH)_2$ and $Mg(OH)_2$, along with CaO and MgO (ranging from 5%, 10%, to 15% by weight), were varied for deposition onto SBA-15C. Subsequently, the impregnated samples underwent drying at a temperature of 110ºC for 18 hours, to ensure the removal of residual moisture.

### 2.3 *Differential scanning calorimetry analysis*

The thermal properties of the impregnated precursors in SBA-15 were characterized using scanning differential calorimetry. This technique was employed to identify the temperature at which specific phase transitions occurred and to determine the temperatures at which the hydroxides and oxides of calcium and magnesium were obtained.

### 2.4 *X-ray Diffraction (XRD)*

The response obtained through this method enables the identification of the diffractogram of crystalline solids Waseda et al. (2011). In this study, XRD was employed, utilizing a D8 Advance Bruker diffractometer, to identify the crystalline phase of the oxides in the adsorbents prepared for $CO_2$ adsorption.

### 2.5 *Desorption adsorption isotherms*

The gas adsorption technique was employed to determine the textural properties of the SBA-15 support material and its variations. $N_2$ adsorption isotherms at 77 K were obtained using an Autosorb-IQ2 instrument (Quantachrome Instruments).

### 2.6 *Thermogravimetric Analysis (TGA)*

Thermogravimetric analysis (TGA), coupled with the derivative thermogravimetry (DTG) technique, was employed to assess the thermal stability of hydroxides and oxides of calcium and magnesium within the pores of mesoporous materials (Montes-Hernandez, *et al*., 2012). The non-isothermal carbonation reaction was conducted using a TGA/DTG thermogravimetric analyzer, specifically a Q500 TGA equipment from TA Instruments. The analysis was performed within a temperature range of 200 °C, with a heating speed of 10 $\frac{^{\circ}C}{min}$ and a flow rate of 50 $\frac{mL}{min}$ of 100% $CO_2$ gas.

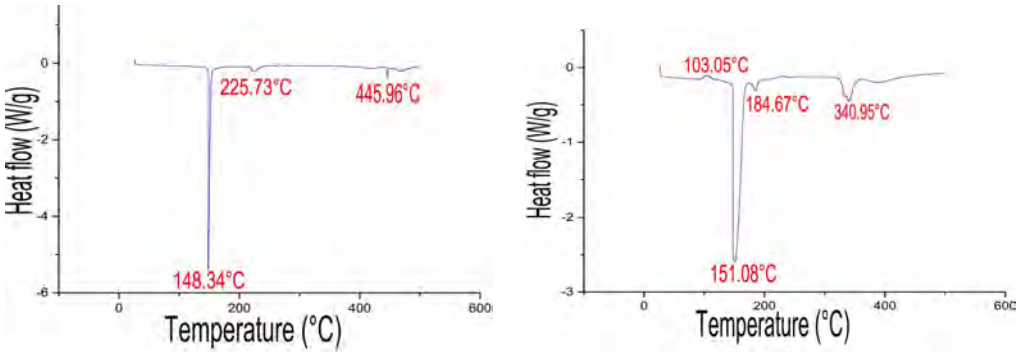


(a) (b)

Figure 2. Profiles of DSC of the hydroxides and oxides precursors of calcium and magnesium.

## 3 Results

### 3.1 Differential Scanning Calorimetry (DSC)

A DSC analysis was applied to the precursors of the hydroxides and oxides of calcium and magnesium after they were impregnated with the SBA-15 and thermally treated at 110 °C. This analysis revealed distinctive peaks for the calcium and magnesium precursors. For the calcium precursor, an endothermic peak was observed at 148.34 °C, corresponding to the formation of hydroxides, and at 445.96 °C, indicative of oxide formation. In the case of the magnesium precursor, an endothermic peak at 151.08 °C signified hydroxide formation, while an additional peak at 340.96 °C corresponded to oxide formation. These results align with existing literature findings (Mureseanu *et al.*, 2023), the results obtained are shown in figure 2.

Specifically, in figure 2(a) the DSC curve demonstrates the acquisition of calcium hydroxides at 148.34 °C, while figure 2(b) shows the formation of magnesium hydroxides at 151.08 °C. The subsequent formation of oxides occurs in the temperature range of 301 °C to 500 °C. In figure 2(a), the DSC curve illustrates the formation of calcium oxides at 445.96 °C, and in figure 2(b), the curve indicates the formation of magnesium oxides at 340.95 °C. It is important to note that this equipment provides temperature values with precision up to two decimal points.

### 3.2 X-ray Diffraction (XRD)

The precursors of Ca and Mg impregnated in SBA-15 underwent a heat treatment at 110 °C for a more precise determination of the temperature at which the hydroxides and oxides of calcium and magnesium are obtained, aligning with existing literature. In Figure 3, the prominent peak centered at 24° in $2\theta$ indicates the presence of amorphous silica, with additional discernible reflections corresponding to CaO and exclusively to MgO. The latter oxides, supported on the surface of SBA-15c, exhibit more observable reflections. However, these reflections are characterized by their weak and broad nature, suggesting that the supported CaO is either amorphous or finely dispersed in nanoparticle dimensions. Determining its exact size, potentially below 5 nm, is challenging due to the potential thickness of the electron beam. Contrastingly, MgO displays reflections that lack well-defined patterns, indicating a high degree of dispersion within SBA-15. This dispersion is advantageous, as a more excellent dispersion of oxide and hydroxide nanoparticles translates to an increased number of active sites for adsorption. The material undergoes drying at 110°C. Notably, the calcium precursor manifests a reflection around 23° and 25° in 2 theta, characteristic of amorphous silica.

The powder X-ray diffraction method was applied to characterize the crystalline phase and structure of SBA-15 samples, calcium and magnesium oxides, and hydroxides. The X-ray diffraction pattern covered a $2\theta$ range between 5 and 60°. Figures 4(a) and 4(b) display the oxides and hydroxides of calcium with the acetate precursor, while figures 4(c) and 4(d) showcase the oxides and hydroxides of magnesium with the same precursor. Figure 4(e) and 4(f) illustrate the oxides and hydroxides of magnesium with chloride as a precursor.

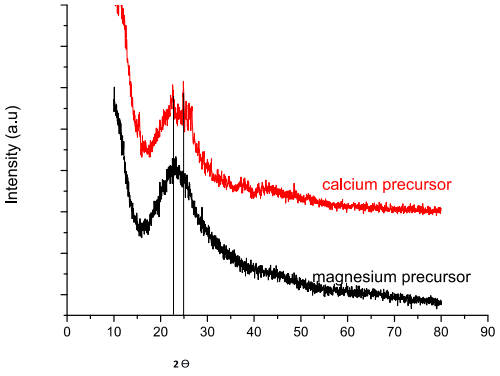


Figure 3. DRX patterns of the precursors of calcium and magnesium.

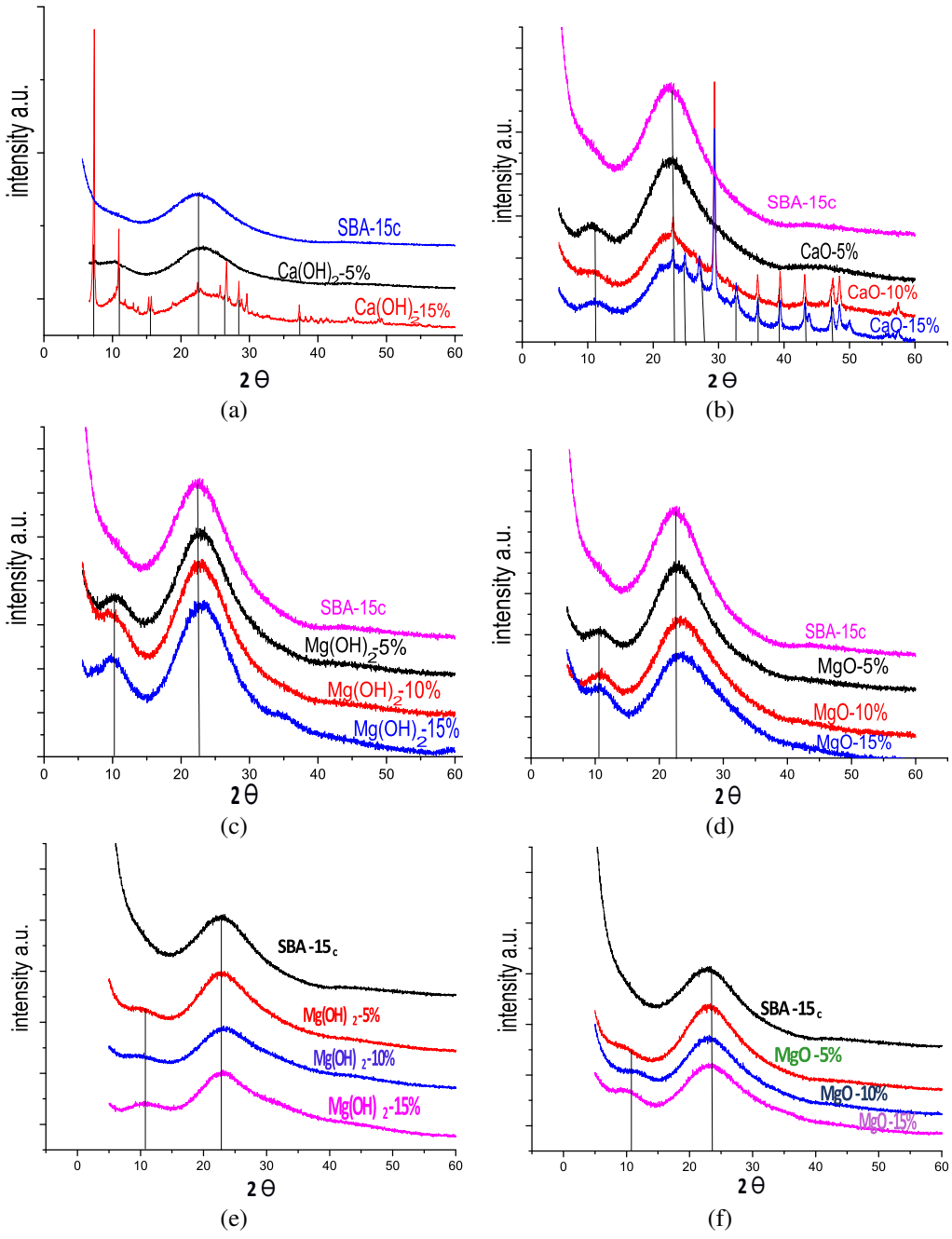


Figure 4. Precursor of acetates. X-ray diffraction (XRD).

In the diffractograms depicting catalysts supported in the oxide state in calcium adsorbents (Figure 4(a) and 4(b), low-intensity peaks are evident at angles $2\theta$ of 25, 28, 32.5, 36, 39, 43, 28, 47, and 50°. These peaks are documented as precursor phases of active sites for catalysis, particularly in the 15% concentration. Magnesium oxides and hydroxides exhibit low-intensity peaks in the 20 to 30° range due to the presence of oxidized transition metal species. This can result from incomplete sulfidation of the oxide state precursor or oxidation of sulfur catalysts before analysis. figure 4(a)/, $Ca(OH)_2$, figure 4(b)/, CaO, figure 4(c)/, $Mg(OH)_2$, figure 4(d)/, MgO. The samples of $Mg(OH)_2$ and MgO do not have well-defined reflections, they are highly dispersed in SBA-15, and this is beneficial because the more dispersed the oxide and hydroxide nanoparticles are, then there will be a greater number of active sites for adsorption, contrary to $Ca(OH)_2$ and CaO. While in the chloride precursor, which is presented as $Mg(OH)_2$ in figure 4(e)/ and MgO in figure 4(f)/, something similar happens in the magnesium acetate precursor. The samples of $Mg(OH)_2$ and MgO do not have well-defined reflections, are highly dispersed in SBA-15, and since the more dispersed the oxide and hydroxide nanoparticles are, the greater the number of active sites for adsorption.

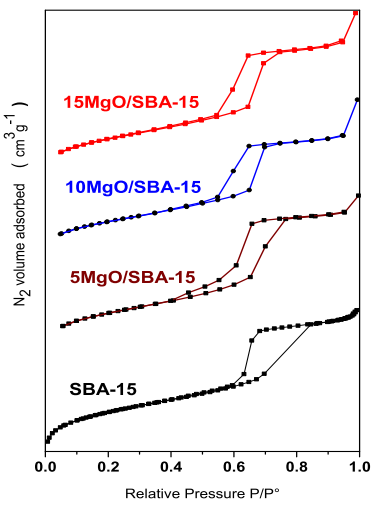


(a)

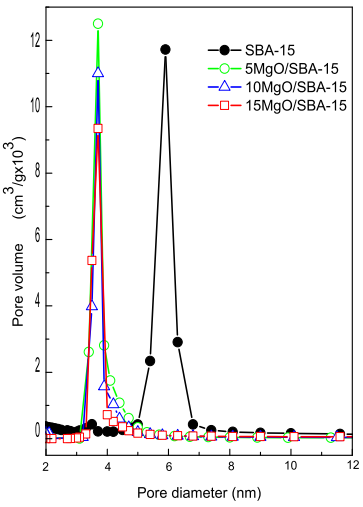


(b)

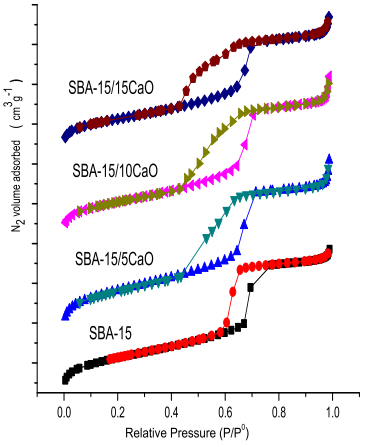


(c)

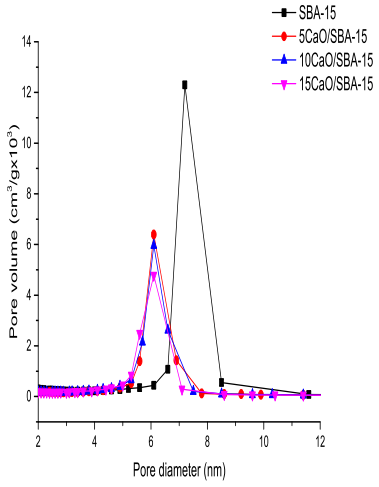


(d)

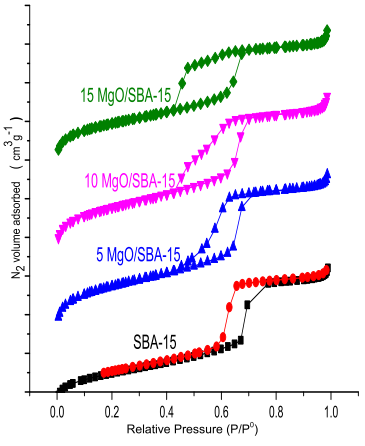


(e)

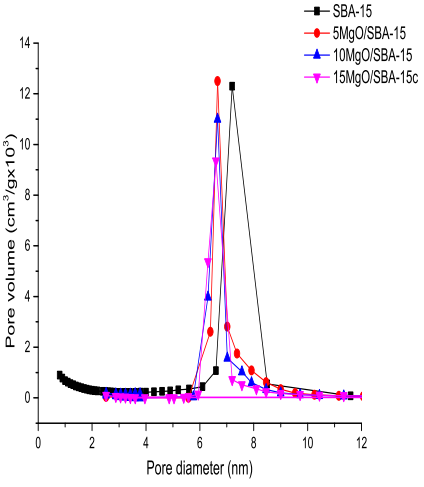


(f)

Figure 5. With the precursor of acetates; MgO isotherms in Figure 5(a)/ Pore size distribution of MgO in Figure 5(b) CaO isotherms in Figure 5(c)/ Pore size distribution of CaO in Figure 5(d) and with chloride precursor; MgO isotherms in Figure 5(e)/ and pore size distribution of MgO in Figure 5(f). There is a change in pore diameter to a smaller diameter following an increase in the load of MgO and CaO, $Mg(OH)_2$ and $Ca(OH)_2$.

The low-intensity diffraction peaks across all samples indicate that most supported species are widely dispersed on the surface of the supports. The presence of less-defined peaks suggests that the supported species are either amorphous or have crystallite sizes below the detection limit of the technique (<4 nm). In figure 4(c), a pronounced reflection, different from that of pure mesoporous silica, indicates the existence of impregnated $Mg(OH)_2$. The same observation holds for MgO in figure 4(d) In figures 4(a) and 4(b), numerous reflections are present, albeit shorter. This suggests that, in all analyzed samples, hydroxides and calcium and magnesium oxides were successfully impregnated. A similar trend is observed in the case of the chloride precursor, which presents magnesium hydroxides in Figure 4(e) and magnesium oxides in figure 4(f). Something similar happens in the precursor of magnesium acetate, as shown in figure 4(e) and 4(f).

### *3.3 $N_2$ adsorption-desorption isotherms and pore size distribution.*

The textural properties of mesoporous materials were investigated through $N_2$adsorption-desorption isotherms at 77 K. Pore size distributions were calculated using the Barrett-Joyner-Halenda model (B.J.H). Figure 5 illustrates the $N_2$ adsorption-desorption isotherms of the materials. All mesoporous samples of MgO / SBA-15 in figure 5(a), SBA-15 and SBA-15 / xCaO, in figure 5(c) with the precursor of acetates and MgO / SBA-15 in figure 5(e), with the precursor of chloride, as well as pure SBA-15, exhibit adsorption isotherms of type IV with areas of hysteresis type H1 according to the IUPAC classification. These isotherms are indicative of mesoporous materials with a hexagonal arrangement of pores.

In Figure 5(a), MgO/SBA-15 with the acetate precursor displays a well-defined hysteresis area at high relative pressures (0.61 <P / P0 <0.8) representing the spontaneous filling of mesopores due to capillary condensation. This indicates the presence of uniform mesopores. Modified mesoporous silicas of MgO exhibit hysteresis areas at lower relative pressure ranges (0.4 <P/P0 <0.7) due to a reduction in mesopore size resulting from the presence of small MgO particles dispersed within SBA-15 pores.

Figure 5(b) illustrates the pore size distribution of adsorbents (SBA-15 and SBA-15/xMgO) with the acetate precursor. The distribution was calculated using desorption isotherm data with the B.J.H. Our mesoporous silica material SBA-15 exhibits a uniform distribution in pore size, centered at approximately 5 nm. The introduction of MgO particles in SBA-15 leads to a reduction in pore size by 1.2 nm. The pore size distributions remain uniform, centering at approximately 3.8 nm, irrespective of the MgO load. These findings suggest that small MgO particles are uniformly dispersed within the pores of SBA-15, indicating that SBA-15 has a high capacity (attributed to high porosity) to disperse MgO particles inside its pores.

Table 1 summarizes the adsorbents' textural properties, including surface area and average pore volume (SBA-15 and SBA-15/xMgO). SBA-15 exhibits a high surface area of 932 $\frac{m^2}{g}$ and a substantial pore volume of 1.05 $\frac{cm^3}{g}$. The incorporation of MgO particles decreases both surface area and total pore volume, which can be attributed to the partial blockage of pores in SBA-15.

In examining MgO-modified adsorbents, it is evident that both surface areas and pore volumes remain high, signifying that SBA-15 facilitates the effective dispersion of MgO nanoparticles. This characteristic indicates a favorable adsorption capacity for $CO_2$ molecules.

When contrasting nitrogen adsorption-desorption isotherms between MgO-free SBA-15 and modified adsorbents containing MgO, a noticeable shift in the turning point of the hysteresis curve to lower relative pressure values (from 0.60 to 0.45) is observed. This shift is attributed to the confinement effect of MgO nanocrystals within the SBA-15 channels.

The CaO/SBA-15 isotherm in figure 5(c) exhibits a well-defined region at high relative pressures (0.6<P/P0<0.8), indicating spontaneous filling of mesopores due to capillary condensation, indicative of uniform mesopores. The nitrogen adsorption-desorption curve for the material resembles that reported in the literature for mesoporous silica material SBA-15 Flodström and Alfredsson (2003). Hysteresis curves for the adsorbents show slight modifications with the incorporation of CaO, suggesting that the mesoporous structure of SBA-15 is preserved even with the incorporation of the highest CaO load (15% by weight).

Figure 5(d), presents the pore size distribution of the adsorbents (SBA-15 and SBA-15/xCaO), with the precursor of acetates. The distribution was calculated with desorption isotherm data using the B.J.H. Our mesoporous silica material SBA-15 shows a uniform distribution in pore size centered at approximately 7.2 nm. Incorporating CaO particles into SBA-15 causes a decrease in pore size of 1.1 nm, as pore size distributions, which are also uniform, are now centered at approximately 6.1 nm, and regardless of CaO charge. These results indicate that small CaO particles have been evenly distributed within the pores of SBA-15, suggesting that SBA-15 has a high capacity (due to high porosity) to disperse CaO particles inside its pores. Table 1 summarizes the textural properties (surface area and average pore volume) of the adsorbents (SBA-15 and SBA-15/xCaO). It

shows that our mesoporous silica material SBA-15 has a high surface area of 819 $\frac{m^2}{g}$ and a high pore volume of 0.964 $\frac{cm^3}{g}$. It can be observed that the incorporation of CaO particles causes a decrease in both the surface area and the total pore volume of SBA-15. This decrease can be explained based on the partial blockage of the pores in SBA-15.

However, the surface areas and pore volumes of CaO-modified adsorbents remain elevated, indicating that SBA-15 promotes the effective dispersion of CaO nanoparticles. These adsorbent materials are anticipated to exhibit a substantial adsorption capacity for $CO_2$ molecules.

Comparing the nitrogen adsorption-desorption isotherms of CaO-free SBA-15 with those of CaO-containing adsorbents reveals a shift in the tipping point of the hysteresis curve to lower values of relative pressure (from 0.60 to 0.45) after CaO loading. This change is likely attributed to the confinement effect of CaO nanocrystals within the SBA-15 channels.

The sample of MgO / SBA-15 in figure 5(e), presents the area of hysteresis in a well-defined range at high relative pressures (0.61 <P / P0 <0.8) that represents the spontaneous filling of the mesopores due to capillary condensation, indicating the presence of uniform mesopores. Modified mesoporous silicas of MgO show areas of hysteresis at lower relative pressure ranges (0.4 <P/P0 <0.7) due to a decrease in mesopore size and to the presence of small MgO particles dispersed within SBA-15 pores.

Figure 5(f) presents the pore size distribution of adsorbents (SBA-15 and SBA-15/xMgO) with the chloride precursor. The distribution, calculated from desorption isotherm data using the B.J.H. method, shows that our SBA-15 mesoporous silica material has a uniform distribution in pore size centered at approximately 7.8 nm. Incorporating MgO particles in SBA-15 leads to a decrease in pore size of 0.8 nm. The pore size distributions, though uniform, are now centered at approximately 7 nm, regardless of the MgO load. These results suggest that small MgO particles are evenly distributed within the pores of SBA-15, highlighting SBA-15's high capacity (attributed to high porosity) to disperse MgO particles within its pores.

Table 1 summarizes the textural properties (surface area and average pore volume) of the adsorbents (SBA-15 and SBA-15/xMgO). Our mesoporous silica material, SBA-15 initially developed by Stucky, exhibits a high surface area of 819 $\frac{m^2}{g}$ and a substantial pore volume of 0.964 $\frac{cm^3}{g}$. The incorporation of MgO particles decreases the surface area and total pore volume of SBA-15, which the partial blockage of pores in SBA-15 can explain.

The surface areas and pore volumes of MgO-modified adsorbents remain elevated, indicating that SBA-15 facilitates the effective dispersion of MgO nanoparticles. These adsorbent materials are anticipated to exhibit a high adsorption capacity for $CO_2$ molecules.

Table 1. Precursors used for the experimentation.

| Precursor | Adsorbent | $S_{BET}$ ($\frac{m^2}{g}$) | Vt ($\frac{cm^3}{g}$) |
|---|---|---|---|
| MgO acetate | SBA-15 | 932 | 1.05 |
| | SBA-15-5MgO | 659 | 0.83 |
| | SBA-15-10MgO | 505 | 0.69 |
| | SBA-15-15MgO | 507 | 0.52 |
| CaO acetate | SBA-15 | 819 | 0.964 |
| | SBA-15-5CaO | 584 | 0.694 |
| | SBA-15-10CaO | 575 | 0.683 |
| | SBA-15-15CaO | 506 | 0.581 |
| MgO chloride | SBA-15 | 819 | 0.964 |
| | SBA-15-5MgO | 634 | 0.74 |
| | SBA-15-10MgO | 593 | 0.707 |
| | SBA-15-15MgO | 521 | 0.674 |

When comparing nitrogen adsorption-desorption isotherms of MgO-free SBA-15 with those of modified adsorbents containing MgO, it was observed that after MgO loading, the inflection point of the hysteresis curve shifts to lower values of relative pressure (from 0.60 to 0.45). This change is likely attributed to the confinement effect of MgO nanocrystals within the SBA-15 channels.

Regarding the pore size distribution shown in Figure 5(b) for MgO with the acetate precursor, figure 5(d) for CaO with the acetate precursor, and figure 5(f), for MgO with the chloride precursor, it is noteworthy that all mesoporous silicas exhibit a uniform and narrow pore size distribution. There is an apparent reduction in pore diameter following an increase in the load of MgO and CaO. Simultaneously, the total volume of $N_2$ decreases with increasing MgO and CaO loading on mesoporous silicas. As expected, introducing magnesium oxide and calcium oxide into the silica matrix decreases the surface area and pore volume of the SBA-15 support, as observed in table 1.

### *3.4 Thermogravimetric Analysis (TGA)*

Figure 6 illustrates the $CO_2$ consumption graph, depicting the carbonation reaction for various adsorbents based on loading calcium and magnesium hydroxides and oxides supported in the SBA-15 matrix.

Figure 6(a) illustrates the calcium oxides in the red graph and magnesium in the black graph, in proportions of 5%, 10% and 15%, in figure 6(b), calcium hydroxides in the black graph, and magnesium in the red graph, in proportions of 5%, 10% and

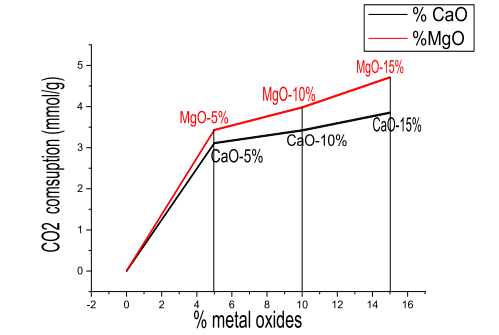


(a)

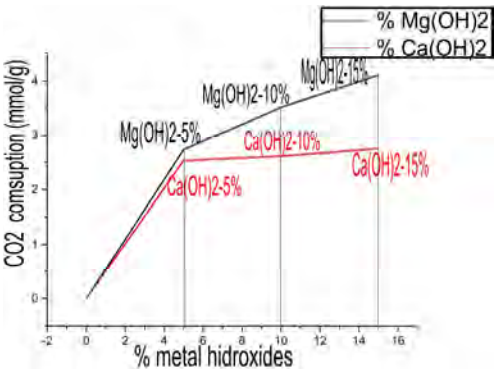


(b)

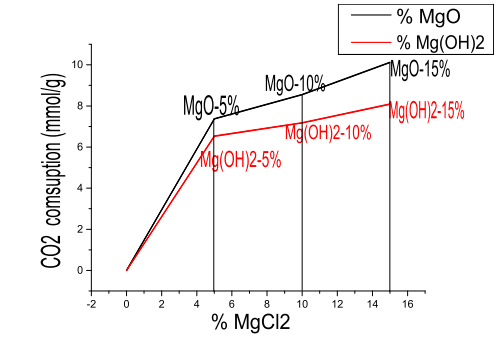


(c)

Figure 6. Adsorption of $CO_2$, using the precursor of acetates.

15%. $CO_2$ adsorption, using the chloride precursor, in figure 6(c), the black graph represents magnesium hydroxides in proportions of 5%, 10% and 15% and the red graph represents magnesium oxides in proportions of 5%, 10% and 15%.

Surface decoration of SBA-15 with nanoparticles of calcium and magnesium hydroxides and oxides generates materials demonstrating $CO_2$ consumption, indicating that these nanoparticles serve as active sites for $CO_2$ adsorption, leading to the carbonation reaction and the formation of $CaCO_3$ and $MgCO_3$.

Figure 6 demonstrates that an incremental increase in the loading of calcium and magnesium hydroxides and oxides in SBA-15 results in a consistent rise in $CO_2$ consumption. This suggests that the elevated loading of these hydroxides and oxides in SBA-15 promotes a more extensive dispersion of nanoparticles, thereby increasing the density of $CO_2$ adsorption sites. Notably, the adsorbent with the highest load of calcium and magnesium hydroxides and oxides (15% by weight of MgO in SBA-15) exhibits the maximum $CO_2$ consumption, indicating a higher concentration of $CaCO_3$.

According to the study's findings, it is evident that the percentage of magnesium oxides and hydroxides impregnation correlates with higher adsorption. Specifically, the highest percentage of $CO_2$ adsorption is observed with a 15% load, demonstrating superior performance for magnesium oxides. In addition, a comparison between 15% magnesium oxides, using acetate and chloride precursors, reveals a more than two-fold difference in $CO_2$ adsorption. In particular, the adsorption is 4.71 $\frac{\text{mmol}}{\text{g}}$ for the acetate precursor and 10.12 $\frac{\text{mmol}}{\text{g}}$ for the chloride precursor, underlining the significant impact of precursor choice on the adsorption efficiency of $CO_2$.

## 3.5 *ESD Analysis and Mapping*

Corroborating the results of the above analyses, in Figure 7 shows the elemental analysis of SBA-15, magnesium and calcium oxides with the acetate precursor, and magnesium oxide with the chloride precursor, showing the presence and dispersion of calcium and magnesium oxides on the surface of SBA-15.

Table 2 shows the mass percentages of calcium and magnesium hydroxides and oxides, with the acetate precursor and the magnesium hydroxides and oxides with the chloride precursor, supported in SBA-15, analyzed by X-ray fluorescence, most of them are higher than the theoretical mass percentages. This is most likely due to the data for surface areas and pore volumes (determined by $N_2$ physisorption at 77K) are probably slightly higher than the actual data.

Table 2. Values of the elemental proportions

| Precursor | Sample | Percentage (%) |
|---|---|---|
| Acetate | MgO-5% | 9.29 |
| | MgO-10% | 15.86 |
| | MgO-15% | 19.27 |
| | $Mg(OH)_2$-5% | 6.88 |
| | $Mg(OH)_2$-10% | 8.28 |
| | $Mg(OH)_2$-15% | 14.15 |
| | CaO-5% | 10.93 |
| | CaO-10% | 23.66 |
| | CaO-15% | 24.31 |
| | $Ca(OH)_2$-5% | 12.99 |
| | $Ca(OH)_2$-10% | 19.14 |
| | $Ca(OH)_2$-15% | 25.96 |

| | | |
|---|---|---|
| Chloride | MgO-5% | 6.24 |
| | MgO-10% | 9.77 |
| | MgO-15% | 12.77 |
| | $Mg(OH)_2$-5% | 4.66 |
| | $Mg(OH)_2$-10% | 7.63 |
| | $Mg(OH)_2$-15% | 13.15 |

## 4 Discussion

According to the results obtained and compared with other articles of $CO_2$ adsorption, the following adsorptions are shown in table 3, for materials at 15% impregnation in mesoporous silica SBA-15.

The mesoporous silica type SBA-15 supports various materials, with magnesium exhibiting notably enhanced $CO_2$ adsorption. The adsorption increases significantly with a higher proportion of impregnation, exemplified by the red graph in figure 6(c) at 15% of MgO chloride precursor, registering 10.12 $\frac{mmol}{g}$. In comparison, the black graph for 15% $Mg(OH)_2$ from the precursor records 8.09 $\frac{mmol}{g}$. This effect is further pronounced when contrasted with the acetate precursor, as evidenced in figure 6(a), where MgO (black graph) reaches 4.71 $\frac{mmol}{g}$ compared to 2.75 $\frac{mmol}{g}$ for CaO (red graph) at 15% acetate precursor and figure 6(b) with $Mg(OH)_2$ (red graph) at 4.11 $\frac{mmol}{g}$ versus 3.85 $\frac{mmol}{g}$ for $Ca(OH)_2$ (black graph). These promising results hold potential for mitigating greenhouse gases, mainly $CO_2$. While acetate precursors exhibit high $CO_2$ adsorption, the chloride precursor demonstrates over double the adsorption for MgO (10.12 $\frac{mmol}{g}$ at 15% compared to the acetate precursor (4.71 $\frac{mmol}{g}$ at 15%).

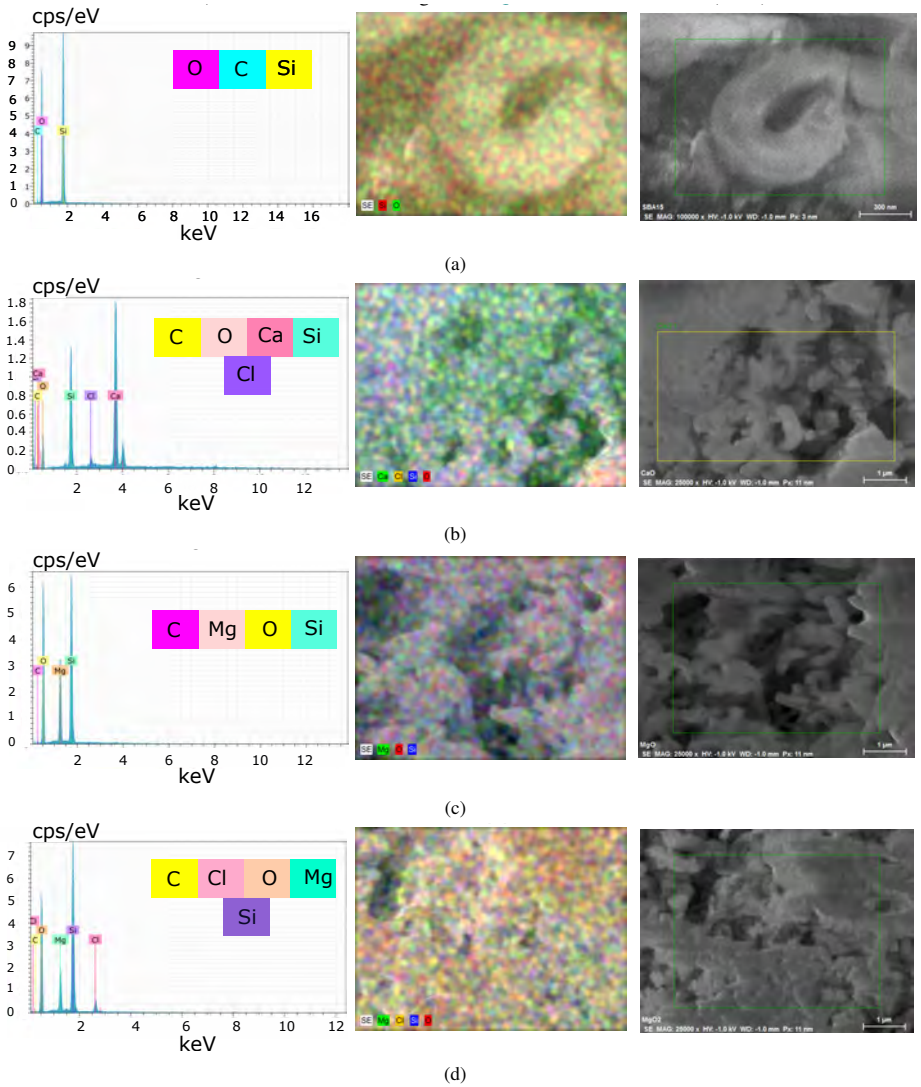


Figure 7. Figure 7(a)/ elemental analysis and mapping of SBA-15, 7(b)/ Elemental analysis and mapping of CaO, with the acetate precursor, 7(c)/ Elemental analysis and mapping of MgO, with the acetate precursor, 7(d)/ Elemental analysis and mapping MgO, with the chloride precursor.

Table 3. $CO_2$ Adsorption over the different synthesized saterials for the case of 15% impregnation on mesoporous silica SBA-15.

| Sample | Forerunner | Adsorption ($\frac{mmol}{g}$) |
|---|---|---|
| $Ca(OH)_2$ | acetate | 2.75 |
| CaO | acetate | 3.85 |
| $Mg(OH)_2$ | acetate | 4.11 |
| MgO | acetate | 4.71 |
| $Mg(OH)_2$ | chloride | 8.09 |
| MgO | chloride | 10.12 |

Table 4. A comparative analysis of $CO_2$ adsorption results reported in the literature for different adsorbent materials.

| Method | $CO_2$ Adsorption ($\frac{mmol}{g}$) | Bibliography |
|---|---|---|
| SBA-15-15MgO | **10.12** | |
| Synthesis of PE-SBA-15 | 0.50-0.85 | Al-Absi *et al.* (2022) |
| Adsorption-desorption | 1.02 | Ai *et al.* (2023) |
| Adsorption-desorption | 1.52 | Maruccia *et al.* (2021) |
| N-CMK-3-750 | 1.55 | Maruccia *et al.* (2023) |
| Synthesis of MA | 1.56 | Wu *et al.* (2022) |
| N-CMK-3-600 | 1.66 | Maruccia *et al.* (2023) |
| Adsorption-desorption | 2.42 | Mohamedali *et al.* (2020) |
| Aluminum impregnation | 5.4 | Guo *et al.* (2022) |

In the case of $Ca(OH)_2$ and CaO with the acetate precursor, $CO_2$ adsorption is 2.75 $\frac{mmol}{g}$ and 3.85 $\frac{mmol}{g}$, respectively. All measurements underwent two repetitions, and the graphs depicted the averages. Noteworthy references include adsorption values of 1.52 $\frac{mmol}{g}$ at 25% humidity (Maruccia *et al.*, 2021), 2.42 $\frac{mmol}{g}$ at 25°C for adsorption and 80°C for desorption (Mohamedali *et al.*, 2020), 0.85 $\frac{mmol}{g}$ at 15% $CO_2$ at 30°C for 150 min (Al-Absi *et al.*, 2022), 1.56 $\frac{mmol}{g}$ at 50°C (Wu *et al.*, 2022), 1.02 $\frac{mmol}{g}$ (Ai *et al.*, 2023), and 4.28 $\frac{mmol}{g}$ at 25°C (Guo *et al.*, 2022). Additionally, the material generated with $Mg(OH)_2$, CaO, $Ca(OH)_2$, and MgO impregnation in SBA-15 demonstrated auspicious results, showcasing potential applications in reducing greenhouse gases, mainly $CO_2$.

The incorporation of nanoparticles of $Mg(OH)_2$, CaO, $Ca(OH)_2$, and MgO onto the surface of the mesoporous matrix SBA-15 was proven effective in generating adsorbents with substantial $CO_2$ adsorption capacity and its conversion to Ca-$CO_3$ through carbonation. These resulting materials, Ca-$CO_3$-SBA-15 and Mg-$CO_3$-SBA-15, hold promise for various applications, including formulations for cementitious materials involved in processes generating significant $CO_2$ emissions. Additionally, the potential design of filters using these adsorbent materials could directly address $CO_2$ emissions from industrial gaseous emissions, offering an exciting alternative for environmental improvement and air quality enhancement.

The analysis was made with the results obtained in the same units of $CO_2$ adsorption that was carried out in the present job ($\frac{mmol}{g}$).
It was analyzed with the highest adsorption obtained from MgO at 15%. The results obtained in this study with 10.12 ($\frac{mmol}{g}$) exceed those reported in the literature.

## Conclusion

The substantial surface area of SBA-15 (819 $\frac{m^2}{g}$), coupled with a high pore volume (0.964 $\frac{cm^3}{g}$) and an optimal mesoporous pore diameter (7.5 nm), facilitated the effective dispersion of $Mg(OH)_2$, CaO, $Ca(OH)_2$, and MgO nanoparticles on its surface. Even with a significant loading of these materials in SBA-15, favorable textural properties were maintained, registering (506 $\frac{m^2}{g}$, 0.581 $\frac{cm^3}{g}$ and 6 nm pore diameter) for the acetate precursor in CaO, (507 $\frac{m^2}{g}$, 0.52 $\frac{cm^3}{g}$ and 4 nm pore diameter) for the acetate precursor in MgO, and (521 $\frac{m^2}{g}$, 0.674 $\frac{cm^3}{g}$ and 7 nm pore diameter) for the chloride precursor in MgO. These properties facilitated a high density of sites conducive to $CO_2$ adsorption. Pure SBA-15 exhibited no $CO_2$ adsorption, underscoring that the nanoparticles of $Mg(OH)_2$, CaO, $Ca(OH)_2$, and MgO serve as active sites for $CO_2$ adsorption, promoting the subsequent carbonation reaction leading to the formation of $CaCO_3$. As the load of $Mg(OH)_2$, CaO, $Ca(OH)_2$, and MgO increased in SBA-15, a consistent rise in $CO_2$ adsorption capacity was observed, resulting in a higher production of $CaCO_3$ on the surface of SBA-15.

Materials exhibiting low-intensity reflections in the X-ray study indicated a high dispersion within SBA-15, a desirable characteristic as increased dispersion of oxide and hydroxide nanoparticles correlates with more active sites for adsorption. This observation aligns with the $N_2$ adsorption-desorption isotherms and pore size distribution results, revealing a reduction in pore diameter and total $N_2$ volume with increasing MgO and CaO load in mesoporous silicas. Notably, magnesium-supported materials displayed the highest $CO_2$ adsorption, with a significant increase proportional to the impregnation, reaching 10.12 $\frac{mmol}{g}$

for 15% MgO chloride precursor and 8.09 $\frac{mmol}{g}$ for 15% $Mg(OH)_2$ the same precursor-more than double the adsorption observed with acetate precursors (4.5 $\frac{mmol}{g}$ and 4.1 $\frac{mmol}{g}$ for 15% MgO and $Mg(OH)_2$, respectively). These results demonstrate the promise of these materials in reducing greenhouse gases, particularly $CO_2$, and suggest potential applications in adsorbing other substances. In conclusion, the study successfully demonstrated that incorporating nanoparticles of $Mg(OH)_2$, CaO, $Ca(OH)_2$, and MgO on the surface of mesoporous matrix SBA-15 generates adsorbents with significant $CO_2$ adsorption capacity and efficient conversion to $CaCO_3$ through carbonation. The resulting materials, $CaCO_3$-SBA-15 and $MgCO_3$-SBA-15, hold the potential for inclusion in cementitious formulations and various applications. Furthermore, designing filters employing these adsorbent materials for direct $CO_2$ adsorption and conversion from industrial gaseous emissions presents an appealing alternative for reducing environmental $CO_2$ emissions and improving air quality. The obtained results, reaching 10.12 $\frac{mmol}{g}$, surpass those reported in the literature, highlighting the effectiveness of the developed materials.

An additional use apart from the cement industry, thanks to the thickness of the silica wall is thick. It has high mechanical, thermal, and hydrothermal resistance, and due to its characteristics, is that it can resist the gases of industries that are often accompanied by water vapor. Not all materials resist it and SBA-15 does. It could be achieved by making silica pellets from calcium and magnesium oxides.

### *Acknowledgements*

We thank Beatriz Millán Malo, Carmen Peza and Manuel Aguilar Franco for the technical support in the characterization techniques and the National Laboratory of Characterization of Materials, for the facilities to carry out the analysis of the samples. We thank as well to Rubén Alejandro García for the aid for LaTex document edition.

## References

Ai, J., Li, F., Wu, Y., Yin, Y., Wu, Z., and Zhang, J. (2023). Synthesis of mesoporous magnesium silicate from coal gangue for efficient $CO_2$ adsorption at room temperature. *Fuel, 341*, 127692. https://doi.org/10.1016/j.fuel.2023.127692

Al-Absi, A., Domin, A., Mohamedali, M., Benneker, A., and Mahinpey, N. (2022). $CO_2$ capture using in-situ polymerized amines into pore-expanded-Sba-15: Performance evaluation, kinetics, and adsorption isotherms. *SSRN Electronic Journal*, page 1. https://doi.org/10.2139/ssrn.4182363

Arbi, H. M., Vijayalakshmi, L., Anil Kumar, Y., Alzahmi, S., Gopi, C. V. V. M., Rusydi, A., and Obaidat, I. M. (2023). A facile two-step hydrothermal synthesis of $CO(OH)_2$@$NiCO_2O_4$ nanosheet nanocomposites for supercapacitor electrodes. *Nanomaterials 13*(13). https://doi.org/10.3390/nano13131981

Beruto, D. and Botter, R. (2000). Liquid-like $H_2O$ adsorption layers to catalyze the $Ca(OH)_2/CO_2$ solid-gas reaction and to form a non-protective solid product layer at 20°C. *Journal of The European Ceramic Society - J EUR CERAM SOC 20*, 497–503. https://doi.org/10.1016/S0955-2219(99)00185-5

Chen, B., Qiu, J., Xu, L., and Cui, Y. (2022). Ni-based mesoporous $Ce_{0.8}Zr_{0.2}O_2$ catalyst with enhanced low-temperature performance for $CO_2$ methanation. *Catalysis Communications 171*, 106515. https://doi.org/10.1016/j.catcom.2022.106515

de Sá da Silva, D. P., de Melo Silva, D. C., Ribeiro, T. R. S., Solano, J. R. S., Barros da Silva, B. J., Altino, S. A., and da Silva, A. O. S. (2022). Mesoporous aluminas synthesis using carboxylic acids to enhance performance in $CO_2$ adsorption. *Journal of Environmental Chemical Engineering*, 10(6):108928. https://doi.org/10.1016/j.jece.2022.108928

Dong, Z., Shi, Y., Jiang, Y., Yao, C., and Zhang, Z. (2023). *In situ* growth of $CsPbBr_3$ quantum dots in mesoporous $SnO_2$ frameworks as an efficient $CO_2$-reduction photocatalyst. *Journal of $CO_2$ Utilization 72*, 102480. https://doi.org/10.1016/j.jcou.2023.102480

Dávila-Parra, F., Plasencia-Jatomea, M., Amaya, O., Mártin-García, A., Vega-Olivas, J., and Almendariz Tapia, F. J. (2022). Influence of initial copper concentration, ph, and cross-linked alginate-chitosan and alginate-chitosan-aspergillus australensis composite beads on the adsorption capacity and removal efficiency of copper ions. *Revista Mexicana de Ingeniería Química 21*, IA2892. https://doi.org/10.24275/rmiq/IA2892

Fadillah, G. and Saleh, T. A. (2022). Advances in mesoporous material for adsorption and photoconversion of $CO_2$ in environmental pollution: Clean environment and clean energy. *Sustainable Chemistry and Pharmacy 29*, 100812. https://doi.org/10.1016/j.scp.2022.100812

Flodström, K. and Alfredsson, V. (2003). Influence of the block length of triblock copolymers on the formation of mesoporous silica. *Microporous and Mesoporous Materials 59*, (2):167–176. https://doi.org/10.1016/S1387-1811(03)00308-1

Gonzales-Condori, E., Avalos-López, G., Gonzales-Condori, J., Mujica-Guzman, A., Terán-Hilares, R., Briceño, G., Quispe-Avilés, J., Parra, P., and Villanueva-Salas, J. (2023). Avocado seed powder residues as a promising bio-adsorbent for color removal from textile wastewater. *Revista Mexicana de Ingeniería Química 22*, IA2370. https://doi.org/10.24275/rmiq/IA2370

Guo, S., Li, Y., Wang, Y., Wang, L., Sun, Y., and Liu, L. (2022a). Recent advances in biochar-based adsorbents for $CO_2$ capture. *Carbon Capture Science & Technology 4*, 100059. https://doi.org/10.1016/j.ccst.2022.100059

Guo, S., Li, Y., Wang, Y., Wang, L., Sun, Y., and Liu, L. (2022b). Recent advances in biochar-based adsorbents for $CO_2$ capture. *Carbon Capture Science & Technology 4*, 100059. https://doi.org/10.1016/j.ccst.2022.100059

Liu, M. and Gadikota, G. (2019). Integrated $CO_2$ capture, conversion, and storage to produce calcium carbonate using an amine looping strategy. *Energy & Fuels 33*, 1722–1733. https://doi.org/10.1021/acs.energyfuels.8b02803

Maruccia, E., Lourenço, M., Priamushko, T., Bartoli, M., Bocchini, S., Pirri, F., Saracco, G., Kleitz, F., and Gerbaldi, C. (2021). Nanocast nitrogen-containing ordered mesoporous carbons from glucosamine for selective $CO_2$ capture. *Materials Today Sustainability 17*, 100089. https://doi.org/10.1016/j.mtsust.2021.100089

Maruccia, E., Piovano, A., Lourenço, M., Priamushko, T., Cavallo, M., Bocchini, S., Bonino, F., Pirri, F., Kleitz, F., and Gerbaldi, C. (2023). Revealing the competitive effect of $N_2$ and $H_2O$ towards $CO_2$ adsorption in n-rich ordered mesoporous carbons. *Journal Materials Today Sustainability 21*, 100270. https://doi.org/10.1016/j.mtsust.2022.100270

Mohamedali, M., Ibrahim, H., and Henni, A. (2020). Imidazolium based ionic liquids confined into mesoporous silica MCM-41 and SBA-15 for carbon dioxide capture. *Microporous and Mesoporous Materials 294*, 109916. https://doi.org/10.1016/j.micromeso.2019.109916

Montes-Hernandez, G., Chiriac, R., Toche, F., and Renard, F. (2012). Gas-solid carbonation of $Ca(OH)_2$ and CaO particles under non-isothermal and isothermal conditions by using a thermogravimetric analyzer: Implications for $CO_2$ capture. *International Journal of Greenhouse Gas Control 11*, 172–180. https://doi.org/10.1016/j.ijggc.2012.08.009

Mureseanu, M., Filip, M., Bleotu, I., Spinu, C. I., Marin, A. H., Matei, I., and Parvulescu, V. (2023). Cu(II) and Mn(II) anchored on functionalized mesoporous silica with Schiff bases: Effects of supports and metal–ligand interactions on catalytic activity. *Nanomaterials 13*, (12). https://doi.org/10.3390/nano13121884

Qin, Z. (2023). Nanostructure design of catalysts: Latest advances and prospects. *Nanomaterials 13*, 1980. https://doi.org/10.3390/nano13121884

Tovar, C., Bonilla-Mancilla, H., Pino-Moreyra, J., Villabona-Ortíz, A., and Ortega-Toro, R. (2020). Effect of the adsorbent dose in Pb(II) removal by using sugar cane bagasse: Kinetics and isotherms. *Revista Mexicana de Ingeniería Química 19*, IA1101. https://doi.org/10.24275/rmiq/IA1101

Tovar, C., Bonilla-Mancilla, H., Villabona-Ortíz, A., Ortega-Toro, R., and Licares-Eguavil, J. (2021). Effect of the adsorbent dose and initial contaminant concentration on the removal of Pb(II) in a solution using opuntia ficus indica shell. *Revista Mexicana de Ingeniería Química 20*, 555–568. https://doi.org/10.24275/rmiq/IA2134

Vakros, J., Hapeshi, E., Cannilla, C., and Bonura, G. (2023). Synthesis, characterization and performance of materials for a sustainable future. *Nanomaterials 13*, 1929. https://doi.org/10.3390/nano13131929

Vance, K., Falzone, G., Pignatelli, I., Bauchy, M., Balonis, M., and Sant, G. (2015). Direct carbonation of $Ca(OH)_2$ using liquid and supercritical $CO_2$: Implications for carbon-neutral cementation. *Industrial & Engineering Chemistry Research 54*,(36), 8908–8918. https://doi.org/10.1021/acs.iecr.5b02356

Villabona-Ortíz, A., Tovar, C., and Ortega-Toro, R. (2019). Modelling of the adsorption kinetics of chromium (vi) using waste biomaterials. *Revista Mexicana de Ingeniería Química 19*, 401–408. https://doi.org/10.24275/rmiq/IA650

Villabona-Ortíz, A., Tovar, C., Ortega-Toro, R., Aguilar-Bermúdez, F., and Pájaro-Moreno, Y. (2021). Synthesis of adsorbents from wheat hulls, extracted cellulose and modified with cetyl trimethyl ammonium chloride to remove congo red in aqueous solution. *Revista Mexicana de*

*Ingeniería Química 20*, IA2426 https://doi.org/10.24275/rmiq/IA2426

Waseda, Y., Matsubara, E., and Shinoda, K. (2011). *X-Ray Diffraction Crystallography*, pages 21–66. https://doi.org/10.1007/978-3-642-16635-8_2 Springer.

Wu, K., Ye, Q., Wang, L., Meng, F., and Dai, H. (2022). Mesoporous alumina-supported layered double hydroxides for efficient $CO_2$ capture. *Journal of $CO_2$ Utilization 60*, 101982. https://doi.org/10.1016/j.jcou.2022.101982